



Cite this: *Soft Matter*, 2019, 15, 2204

## Understanding the mechanical link between oriented cell division and cerebellar morphogenesis

Emma Lejeune,<sup>ib \*ab</sup> Berkin Dortdivanlioglu,<sup>ib a</sup> Ellen Kuhl<sup>ib c</sup> and Christian Linder<sup>ib ac</sup>

The cerebellum is a tightly folded structure located at the back of the head. Unlike the folds of the cerebrum, the folds of the cerebellum are aligned such that the external surface appears to be covered in parallel grooves. Experiments have shown that anchoring center initiation drives cerebellar foliation. However, the mechanism guiding the location of these anchoring centers, and subsequently cerebellar morphology, remains poorly understood. In particular, there is no definitive mechanistic explanation for the preferential emergence of parallel folds instead of an irregular folding pattern like in the cerebral cortex. Here we use mechanical modeling on the cellular and tissue scales to show that the oriented granule cell division observed in the experimental setting leads to the characteristic parallel folding pattern of the cerebellum. Specifically, we propose an agent-based model of cell clones, a strategy for propagating information from our *in silico* cell clones to the tissue scale, and an analytical solution backed by numerical results to understand how differential growth between the cerebellar layers drives geometric instability in three dimensional space on the tissue scale. This proposed mechanical model provides further insight into the process of anchoring center initiation and establishes a framework for future multiscale mechanical analysis of developing organs.

Received 1st November 2018,  
Accepted 3rd February 2019

DOI: 10.1039/c8sm02231c

rsc.li/soft-matter-journal

## 1 Introduction

The cerebellum is a major feature of the vertebrate brain and is important for functions such as coordination, cognition, and muscular activity.<sup>1</sup> The fully developed cerebellum exhibits a complex three-dimensional structure where the folded cerebellar cortex externally appears as finely spaced parallel grooves, shown in Fig. 1b.<sup>2</sup> Understanding the development of these cerebellar folds, referred to as folia, is an active area of research. Initially, during development, the surface of the cerebellum is smooth. The folia of the cerebellum then arise hierarchically following a tightly coordinated sequence of genetically regulated events.<sup>3–5</sup> At the start of foliation, structures termed anchoring centers form at the base of each fissure. Once these anchoring centers are established, they limit granule cell progenitor dispersion, which contributes to the spatial heterogeneity of different folia.<sup>6</sup> Although the importance of these anchoring centers is known, the mechanism triggering the location and timing of anchoring center initiation is not fully understood.<sup>5</sup> Recent work has suggested that anchoring center initiation is driven by

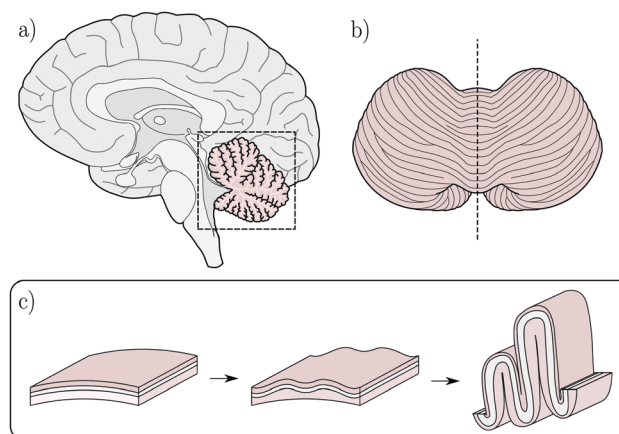


**Fig. 1** (a) Sagittal section of the brain with the cerebellum highlighted; (b) external view of the cerebellum in the coronal plane, note the anisotropy in the foliated pattern; (c) illustration of the foliation mechanism: initially anchoring centers form on an un-patterned surface which subsequently develops potentially heterogeneous folds with anchoring centers at the base.

<sup>a</sup> Department of Civil and Environmental Engineering, Stanford University, Stanford, CA, USA

<sup>b</sup> Institute for Computational Engineering & Sciences, The University of Texas at Austin, Austin, TX, USA. E-mail: elejeune@utexas.edu

<sup>c</sup> Department of Mechanical Engineering, Stanford University, Stanford, CA, USA

tissue-scale mechanical forces that arise due to differential growth.<sup>7,8</sup> In our previous work, we proposed growth-induced surface wrinkling as a plausible explanation for anchoring center initiation.<sup>7</sup> This idea follows from many other examples of mechanical instability driving organ morphogenesis,<sup>9–12</sup>

including in the cerebrum.<sup>13–17</sup> However, to the author's knowledge, there has been limited exploration of mechanically driven morphogenesis in the cerebellum to date.<sup>7,8,18,19</sup>

In this work, we focus on a simple question: how does the orientation of cell division influence anchoring center initiation? From the experimental literature, we know that granular cells in the external granular layer divide preferentially but not exclusively in the anterior–posterior (A–P) direction at a much higher rate than cells in the internal granular layer.<sup>6</sup> What is unknown, is how specifically this oriented cell division may lead to uniaxial folia, particularly in the context of geometric instability driven by differential growth. Multi-scale mechanical modeling offers a unique opportunity to explore this link. We approach this problem with two models. Our first model is an agent-based model of granule cell progenitor clones where cell growth and division algorithms are motivated by experimental results from the literature. We introduce a strategy for post-processing the cellular-scale agent-based model results such that they feed into the second tissue-scale model which treats the cerebellum as a continuum. In our second model, we study the influence of physically realistic anisotropic growth on surface wrinkling. This is done through both incremental stability analysis<sup>20</sup> and numerical modeling with isogeometric analysis.<sup>21</sup> By approaching this problem with fully three-dimensional models, we are able to study how the symmetry of the cerebellum emerges, rather than treating this symmetry as inherent and only presenting a model in two-dimensional space. The three-dimensional model also offers a better platform for future comparison to the developing cerebrum where different cellular scale behavior leads to different morphology on the tissue scale.

The remainder of the paper is organized as follows. In Section 2, we discuss our methods for computational modeling

of cell clones, connecting cell clone models to the tissue scale, and predicting the onset of the wrinkling instability with anisotropic film growth. In Section 3, we show representative simulation and analytical results and discuss the implications for cerebellar morphogenesis. Concluding remarks are given in Section 4.

## 2 Methods

An overview of the computational framework presented here is illustrated in Fig. 2. In Section 2.1, we describe the features of our agent-based cell model that are matched to experimental observations. Then, in Section 2.2, we describe our procedure for post-processing the agent-based model to inform macro-scale behavior. Finally, in Section 2.3, we describe our macro-scale model for understanding the buckled mode shape at the onset of geometric instability.

### 2.1 Computational modeling of cell clones

Agent-based cell models are a class of computational models where the actions and interactions of individual cells are prescribed by algorithmic rules. With this structure, collective system behavior is free to emerge.<sup>22</sup> In this work, we use a mechanically driven agent-based modeling framework where mechanical equilibrium is maintained by satisfying the peridynamic equation of motion.<sup>23</sup> Further details of this broader framework are available in Appendix A.1 and our previous publication.<sup>24</sup> In the remainder of this section, we will describe the algorithmic rules implemented to capture experimental observations from the literature related to cell growth and cell division in the external granule layer of the developing cerebellum.

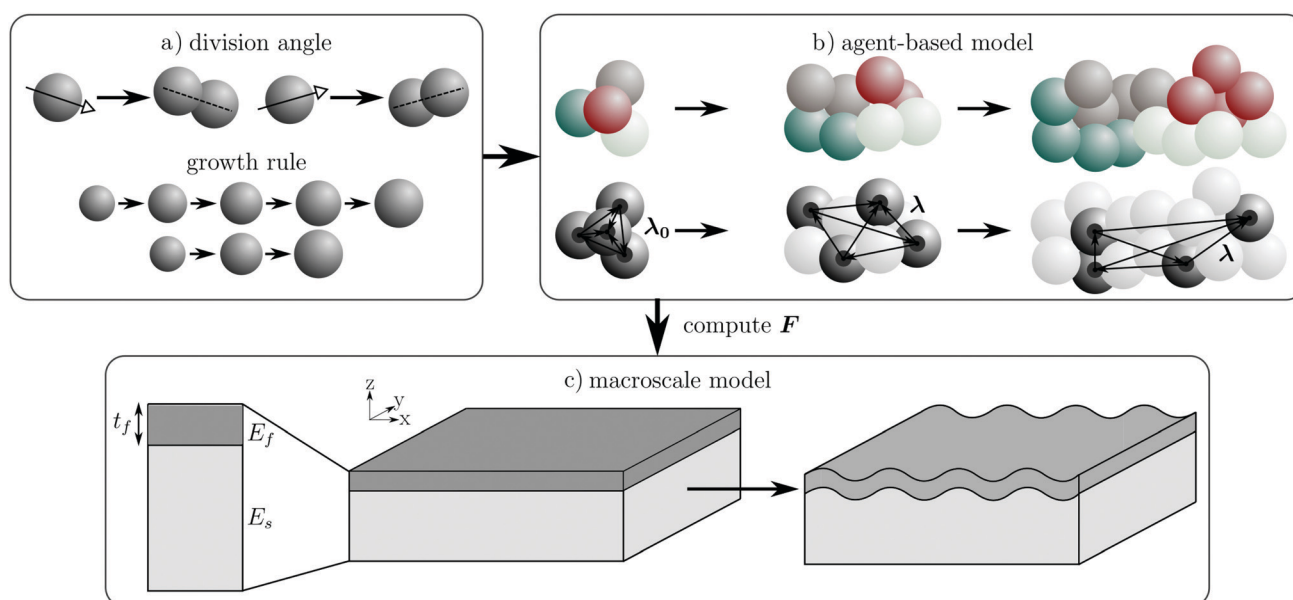


Fig. 2 (a) Individual instances of cell division angle and growth rate are drawn from probability distributions in a manner consistent with experimentally observed behavior; (b) cells are modeled in an agent-based setting and agent-based simulations are post-processed to convey information to the macroscale; (c) macroscale continuum modeling predicts the buckled mode shape at the onset of geometric instability.

First, we consider the cell growth algorithm. In the developing cerebellum, the results of experimental clonal analysis indicate that the cells are not growing in sync.<sup>6,25</sup> In the computational setting, synchrony is the default behavior. Therefore, we need to prescribe cell growth such that cells will grow and divide asynchronously. To do this, we begin each simulation with cells that are non-uniform initial sizes. Each cell  $i$  will have an initial radial growth value of  $g_i$  randomly computed as

$$g_{\min} = 0 \quad g_{\max} = \sqrt[3]{2} - 1.0 \quad g_i \sim \mathcal{U}(g_{\min}, g_{\max}) \quad (1)$$

where  $g_{\max}$  is the size at which cells will divide, and  $\mathcal{U}$  is the uniform distribution. The growth rate  $r_i$  of each cell  $i$  is then generated from a probability distribution as

$$r_i \sim \mathcal{N}(r_{\text{mean}}, r_{\text{std}}) \quad \text{if } r_i < r_{\min} \rightarrow r_i := r_{\min} \quad (2)$$

where  $\mathcal{N}$  is the normal distribution. Radial growth is then applied to cell  $i$  as

$$g_i^{t+1} = g_i^t + r_i. \quad (3)$$

With this algorithm,  $r_i$  remains constant for the entirety of one cell cycle, and cells with higher values of  $r_i$  grow at a faster rate. The combination of different initial sizes and growth rates leads to overall asynchronous population growth, which is consistent with experimental observations. In future work, more specific and biologically realistic algorithmic rules to describe cell growth throughout the cell cycle can be implemented in this framework.

In Fig. 3, we show that our chosen algorithm results in asynchronous growth for a population of 200 cells arising from a single cell. We measure synchrony by adapting a technique available in the literature that relies only on tracking the change in number of cells  $\Delta\text{CN}$ .<sup>26</sup> We plot  $\Delta\text{CN}$  between step  $k - 1$  and  $k$  defined as

$$\Delta\text{CN} = \log_2 \text{CN}_k - \log_2 \text{CN}_{k-1} \quad (4)$$

and the associated moving maximum over a window equivalent to one cell cycle. If the cells were dividing perfectly in sync,

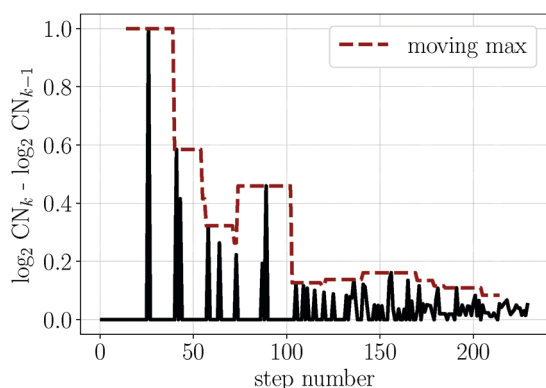


Fig. 3 Consistent with experimental results, we implement unsynchronized cell population growth with  $r_{\text{mean}} = 0.01$ ,  $r_{\text{std}} = 0.005$ , and  $r_{\min} = 0.001$ . We test the population level synchrony by examining the change in cell number per step.<sup>26</sup> Here, we plot the moving maximum with a window of one average cell cycle.

the moving maximum of  $\Delta\text{CN}$  would remain equal to 1. From the plot in Fig. 3, it is clear that the moving maximum decreases sufficiently such that the growth algorithm is asynchronous.

Next, we consider the cell division algorithm. When cells divide, they divide in a specified direction. In three-dimensional space, this is represented as a unit vector  $\mathbf{x}$ . We treat  $\mathbf{x}$  as a random variable drawn from an underlying probability distribution. Hypothetically, this could be an empirical distribution that follows directly from experimental data. However, there is presently insufficient information available from experiments to meaningfully do this. What is known from experiments is that the direction of cell division in the developing cerebellum is not uniform, and that the division plane (division angle is the normal vector of the division plane) is more likely to be perpendicular than parallel to the anterior-posterior axis though it is not exclusively in a single orientation. To capture this behavior in a highly simplified manner, we choose a three-dimensional von Mises–Fisher probability distribution written as

$$f(\mathbf{x}; \mu, \kappa) = \frac{\kappa}{4\pi \sinh \kappa} \exp(\kappa \mu^T \mathbf{x}) \quad (5)$$

where  $\kappa > 0$  is the concentration parameter and  $\mu$  is the mean direction set as a unit vector  $\mu = [1, 0, 0]^T$ .<sup>27</sup> With  $\kappa \rightarrow 0$ , this approaches a spherical uniform distribution. The expression  $1/\sqrt{\kappa}$  is analogous to the standard deviation in a normal distribution. In the numerical setting, we generate random vectors  $\mathbf{x}$  with the Ulrich–Wood algorithm.<sup>28,29</sup> To visualize this distribution in a manner similar to reported experimental observations,<sup>6</sup> we plot the distribution of the division plane for sagittal, coronal, and transverse cuts with 100 000 simulated random variables in Fig. 4. From comparing Fig. 4 to the experimental results reported in Legué *et al.*,<sup>6</sup> we find that a simulated distribution with a value of  $\kappa \approx 2$ –4 is most relevant to the developing cerebellum. In Section 3, we will show representative simulation results with different values of  $\kappa$ .

## 2.2 Connecting the results of the cell clone model to the tissue scale model

On the tissue scale, we treat the cerebellum as a continuum. In our continuum model, we implement tissue growth simply as a growth-induced deformation gradient  $\mathbf{F}$ . To do this, we adapt our recently proposed technique of computing an approximate deformation gradient  $\mathbf{F}$  from the results of a discrete agent-based model.<sup>30</sup> The basic set up for this approach is illustrated in Fig. 2b. We compute  $\mathbf{F}$  from our agent-based model by tracking the change in position of cells from the start to end of the simulation. Essentially, we treat all cells that are present at the start of the simulation as fiducial markers. When the fiducial marker cells divide, fiducial marker status is passed to one of the resulting daughter cells at random. This is shown in Fig. 2b where the darker cells represent the fiducial marker cells. We analyze the change in position of these cells in a post-processing step as follows.

For each fiducial marker  $j$  in  $j = \{1 \dots m\}$ , consider all marker pairs  $j$ – $k$  that connect marker  $j$  to markers  $k$  in  $k = \{1 \dots m\}$ ,  $k \neq j$ .

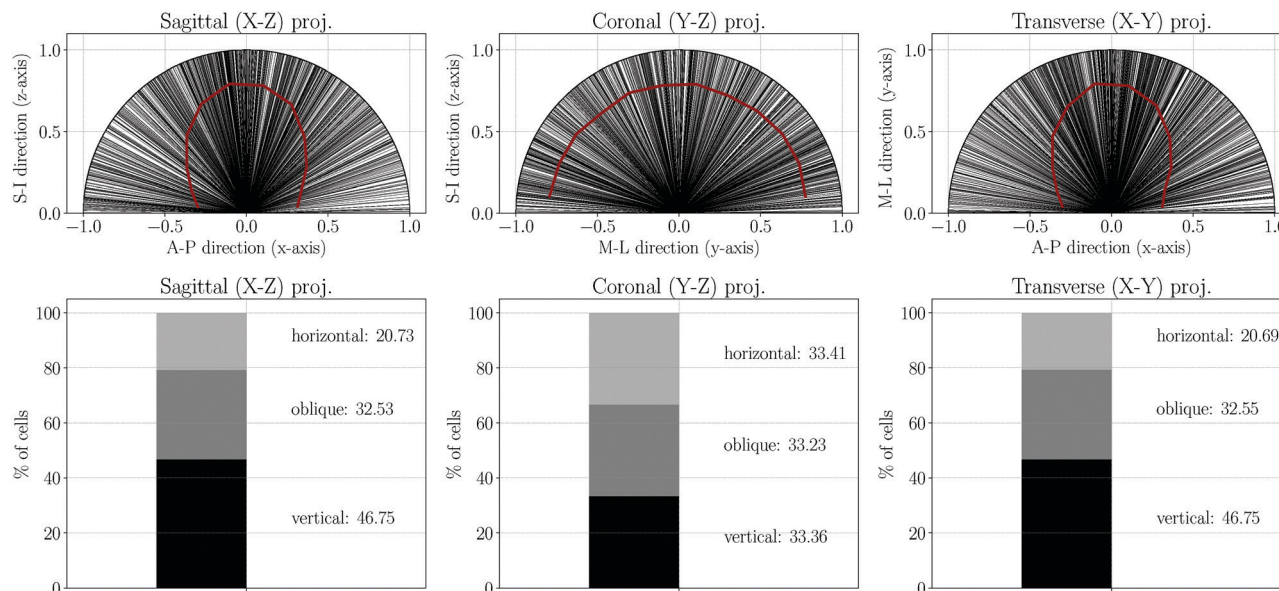


**Fig. 4** Consistent with experimental results, we implement a non-uniform division direction distribution. For a three-dimensional von Mises-Fischer distribution with  $\mu = [1, 0, 0]^T$  and  $\kappa = 2.0$ , we examine the distribution of observed division planes projected onto two-dimensional cuts in the sagittal, coronal, and transverse directions. In the lower row, “horizontal” refers to division planes with angles  $0^\circ$ – $30^\circ$ , “oblique” refers to division planes with angles  $30^\circ$ – $60^\circ$ , and “vertical” refers to division planes with angles  $60^\circ$ – $90^\circ$  in the two-dimensional axis of the cut. The solid red line in the upper plots is proportional to the empirical probability density of the simulated distribution. The information is presented this way such that it is possible to roughly compare the chosen simulation distribution to experimentally observed behavior.<sup>6</sup>

With these  $n = m(m - 1)/2$  pairs, we consider pair-connecting stretch vectors  $\lambda_0$  at the start of the simulation and  $\lambda_t$  at each subsequent simulation step  $t$ . Then, we define an array of initial stretch vectors  $\Lambda_0$  and an array of current stretch vectors  $\Lambda_t$  as

$$\Lambda_0 = [\lambda_0^1 \lambda_0^2 \dots \lambda_0^m] \quad \Lambda_t = [\lambda_t^1 \lambda_t^2 \dots \lambda_t^m] \quad (6)$$

where both arrays have dimension  $3 \times n$ . Then, we introduce the approximate growth-induced deformation gradient at step  $t$   $F_t$  with dimension  $3 \times 3$  to relate these two matrices as

$$F_t \Lambda_0 = \Lambda_t. \quad (7)$$

This results in an over-determined system of equations where we can solve for the best-fit for  $F_t$  as

$$F_t = \Lambda_t \Lambda_0^T (\Lambda_0 \Lambda_0^T)^{-1}. \quad (8)$$

Notably, this simple post-processing procedure relies only on the ability to track the change in position of cell centers. This means that it can be readily applied to other agent-based models. Future advances in experimental techniques and cell tracking methodology may eventually allow this procedure to be applied directly to experimental data.<sup>31</sup>

### 2.3 Tissue scale modeling of the wrinkling instability

On the tissue scale, we treat the developing cerebellum as a continuous block of material. The goal is to understand the onset of geometric instability driven by the compression that arises due to differential growth between the internal and external layers. This is similar to our previous work, where we modeled the cerebellum as a two-dimensional tri-layer system

where the top layer represented the external granular layer, the intermediate layer represented the Purkinje cell layer, and the bottom layer represented the internal granule cell layer.<sup>7</sup> In our previous work, we showed that wrinkling will occur with the external granular layer acting as a film and the combined soft Purkinje layer and internal granular layer acting as a substrate. In this paper we are interested in understanding buckling behavior in the full three-dimensional case, without making the limiting assumption that the buckling mode must be uniaxial. To do this, we model the cerebellum as a three-dimensional bi-layer where the film represents the rapidly growing external granular layer and the substrate approximates the combined internal layers, with a combined stiffness lower than the stiffness of the film, illustrated in Fig. 2. Then, we study this system analytically *via* an incremental stability analysis and numerically by tracking the stability of isogeometric analysis (IGA) simulations. In this work, we are concerned with the onset of the instability and the initial buckling pattern, and we do not delve into post-buckling behavior. In this regime, we can study the onset of the instability with an elastic material model while the assumption of elastic material behavior is likely violated in the post-buckling regime.<sup>8,18</sup>

First, we define the deformation gradient  $\mathbf{F} = \nabla_{\mathbf{x}}\varphi$  where  $\varphi$  maps points from the undeformed configuration  $\mathbf{X}$  to the deformed configuration  $\mathbf{x}$ . In the analytical setting,  $\mathbf{F}$  is homogeneously applied to the whole bi-layer domain through essential boundary conditions. In the numerical setting, we multiplicatively decompose the deformation gradient as  $\mathbf{F} = \mathbf{F}^e \mathbf{F}^g$  where  $\mathbf{F}^e$  is the elastic component and  $\mathbf{F}^g$  is the growth

component, and apply  $\mathbf{F}^g$  either homogeneously to both film and substrate (analogous to the compression at the boundaries case) or exclusively to the film. In our incremental stability analysis, we study the system where both the film and substrate experiences in-plane compression such that homogeneous elastic deformation of the system is simply defined as  $\mathbf{F}$ . Because this is not entirely identical to the case of differential growth,<sup>32</sup> we compare the incremental stability analysis to numerical results that reflect both the case of homogeneous compression and the case of differential growth in Section 3.2. Based on the agent-based simulations that will be discussed in more detail in Section 3.1, we focus on transversely isotropic compression.

To begin the incremental stability analysis, we consider a perturbation  $\mathbf{u}$  defined as an incremental deformation superimposed on a finite deformation  $\mathbf{x}$ .<sup>20</sup> The finite deformation  $\mathbf{x}$  is defined such that it already satisfies the equilibrium equations. The deformation gradient including  $\mathbf{u}$  is written as

$$\bar{\mathbf{F}} = \frac{\partial(\mathbf{x} + \mathbf{u})}{\partial\mathbf{X}} = \mathbf{F} + \frac{\partial\mathbf{u}}{\partial\mathbf{X}} \rightarrow \delta\mathbf{F} = \frac{\partial\mathbf{u}}{\partial\mathbf{X}}. \quad (9)$$

We then obtain a first order approximation of the incremental free energy using a power series expansion around  $\delta\mathbf{F}$  as

$$\bar{\psi}(\bar{\mathbf{F}}) = \psi(\mathbf{F}) + \frac{\partial\psi}{\partial\mathbf{F}} : \delta\mathbf{F} + O(\delta^2) \quad (10)$$

where  $\psi$  is the free energy function for an incompressible neo-Hookean material defined as

$$\psi(\mathbf{F}) = W(\mathbf{F}) - pG(J) \quad (11)$$

with  $W(\mathbf{F})$  as the elastic contribution,  $J = \det\mathbf{F}$ , and  $p$  as the Lagrange multiplier included to enforce incompressibility. Neglecting the higher order terms in eqn (10) and accounting for  $p \rightarrow p + \delta p$  in eqn (11), the constitutive relation is derived from the free energy  $\bar{\psi}(\bar{\mathbf{F}})$  as

$$\bar{\mathbf{P}} = \frac{\partial\bar{\psi}}{\partial\bar{\mathbf{F}}} \quad (12)$$

where  $\bar{\mathbf{P}}$  is the first order approximation of the first Piola–Kirchhoff stress tensor for the perturbed deformation. The total first Piola–Kirchhoff stress is then defined as  $\bar{\mathbf{P}} = \mathbf{P} + \delta\mathbf{P}$ , and computing the increment  $\delta\mathbf{P}$  results in the equation

$$\delta\mathbf{P} = \frac{\partial^2 W}{\partial\mathbf{F}^2} : \delta\mathbf{F} - \delta p\mathbf{F}^{-T} + p\mathbf{F}^{-T}\delta\mathbf{F}^T\mathbf{F}^{-T} \quad (13)$$

where the incompressibility of the material (typical for modeling soft biological tissue) results in the constraint

$$\delta J = \text{tr}(\mathbf{F}^{-T}\delta\mathbf{F}) = 0. \quad (14)$$

By definition,  $\text{Div}\mathbf{P} = 0$  is automatically satisfied by the solution  $\mathbf{x}$ . Therefore, the governing equilibrium equation can be concisely written as

$$\text{Div}\delta\mathbf{P} = 0. \quad (15)$$

Given this set up, we assume a general form of the solution in the film for  $\mathbf{u}$  and  $p$  as

$$\begin{aligned} u_1 &= Ae^{rX_3} \sin(kX_1) \cos(\rho X_2) \\ u_2 &= Be^{rX_3} \cos(kX_1) \sin(\rho X_2) \\ u_3 &= Ce^{rX_3} \cos(kX_1) \cos(\rho X_2) \\ p &= \mu De^{rX_3} \cos(kX_1) \cos(\rho X_2). \end{aligned} \quad (16)$$

The exponential dependence in the  $X_3$  direction allows the sinusoidal perturbation to decay in the substrate as  $X_3 \rightarrow -\infty$ . Then, we use eqn (14), eqn (15), and the appropriate boundary conditions to solve numerically for strain and mode shape at the onset of the instability for a given film–substrate stiffness ratio, film thickness  $h$ , and a desired form of  $\mathbf{F}$ . Further details of this procedure are given in Appendix A.2. Representative results of this analysis are presented in Section 3.2. As noted previously, the compression case is not perfectly equivalent to the differential growth case. To address this, we also conduct numerical simulations using isogeometric analysis where the instability is driven by inhomogeneous differential growth<sup>33</sup> and compare the results of these simulations to our analytical solution.

## 3 Results and discussion

There are two main results from implementing our models. First, in a manner consistent with predictions from experimental observations,<sup>6</sup> we are able to demonstrate that oriented cell division leads to anisotropic population growth. These results are presented in Section 3.1. Second, we are able to show that the anisotropic growth that arises from oriented cell division leads to a uniaxial mode of geometric instability consistent with cerebellar morphology. These results are presented in Section 3.2.

### 3.1 Oriented cell division leads to three-dimensional anisotropic population growth

In Section 2.1, we introduced our agent-based model with asynchronous growth and oriented cell division. In Fig. 5, we show the qualitative results of simulations where a population of cells arises from a single initial cell. In this figure, we plot all of the daughter cells that arise from the first four cells with the same color to maintain an analogy to experimental clonal analysis. From these qualitative results, it is already clear that as the underlying probability distribution of cell division angle becomes more oriented, modeled by increasing  $\kappa$ , population growth becomes more uni-directional anisotropic.

Next, we quantitatively investigate our agent-based model with the method described in Section 2.2. To do this, we begin with a  $3 \times 3 \times 3$  block of 27 cells, and then grow and divide the cells according to the prescribed rules until the cell population has doubled. By tracking the change in position of these cells, we are able to compute an approximate deformation gradient  $\mathbf{F}$  at every step of the simulation. For an individual simulation, the discrete nature of cell division and the non-uniform growth

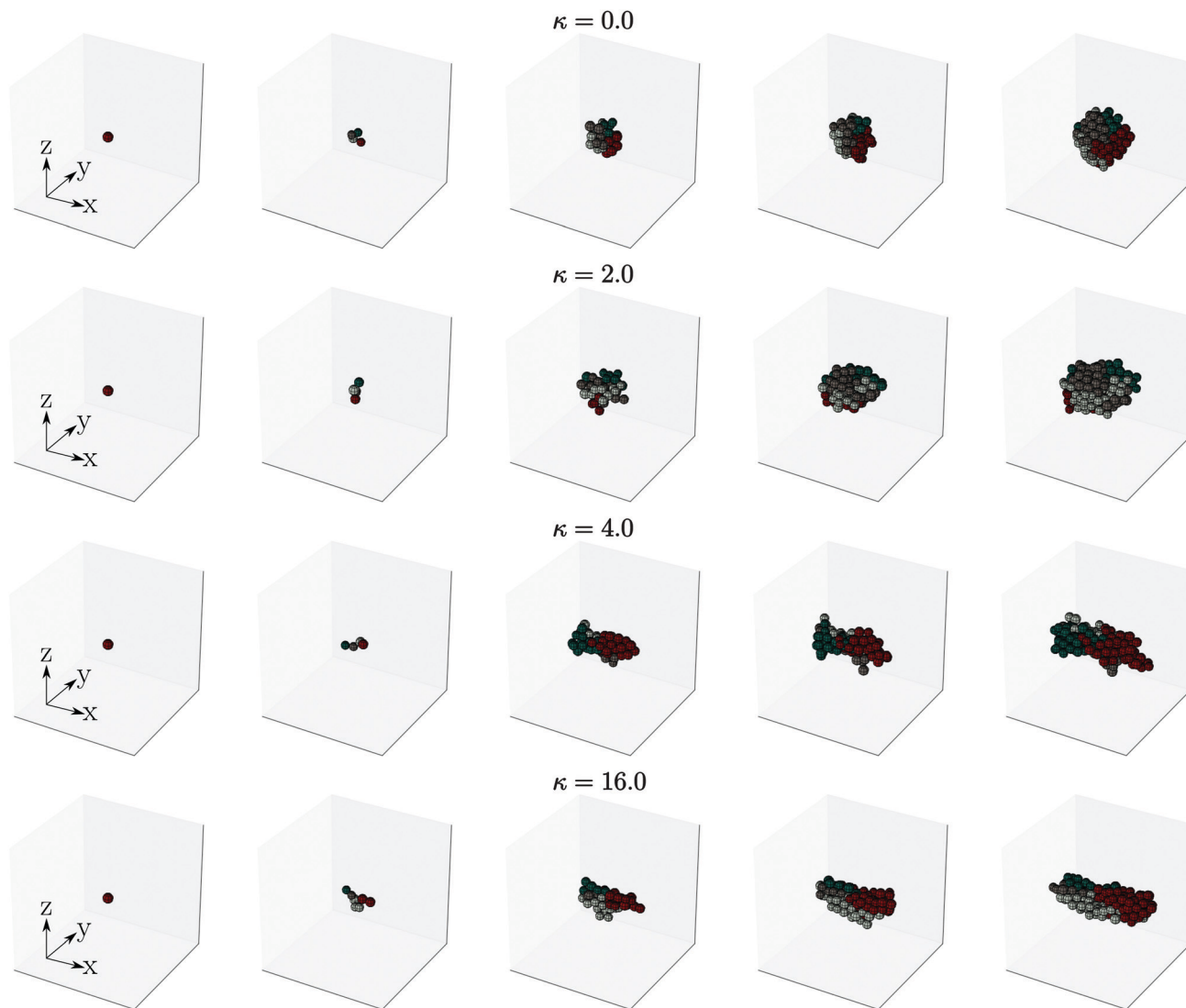


Fig. 5 Illustration of growing cell populations with non-synchronous growth and von Mises–Fisher division angle distributions. After the second round of cell division (4 daughter cells) all future daughter cell generations are plotted with the same color. As  $\kappa$  increases, population growth becomes more uni-directional anisotropic. This figure illustrates *in silico* clonal analysis.

rates will lead to changes in  $\mathbf{F}$  that are generally neither smooth nor monotonic. However, when we consider average behavior across several simulations, we can clearly observe smooth and monotonic changes in  $\mathbf{F}$  as the cell population grows. This averaged behavior is most physically relevant to propagating information from the cellular scale to the tissue scale.

In Fig. 6, we show quantitatively how population growth is influenced by oriented cell division. In the plot where  $\kappa = 0.0$ , we see that  $F_{xx} = F_{yy} = F_{zz}$ . Therefore, population growth is isotropic and  $\mathbf{F}$  can be represented as

$$\mathbf{F} = \mathbf{I} + \eta \mathbf{e}_1 \otimes \mathbf{e}_1 + \eta \mathbf{e}_2 \otimes \mathbf{e}_2 + \eta \mathbf{e}_3 \otimes \mathbf{e}_3 \quad (17)$$

where  $\eta$  is a constant. When  $\kappa$  is high, for example the plot where  $\kappa = 16.0$ , population growth approaches transverse isotropy and  $\mathbf{F}$  can be represented as

$$\mathbf{F} = \mathbf{I} + \eta \mathbf{e}_1 \otimes \mathbf{e}_1 \quad (18)$$

where  $\mathbf{I}$  is the identity tensor,  $\eta$  is a constant, and  $\mathbf{e}_1$  is a basis vector. However, the behavior that most closely resembles that of the developing cerebellum is observed in an intermediate range of  $\kappa$  values. In Fig. 6,  $\kappa = 1.0$ ,  $\kappa = 2.0$ ,  $\kappa = 4.0$ , and  $\kappa = 6.0$  are representative intermediate values. For these cases, population growth is neither fully isotropic nor transversely isotropic. Instead,  $\mathbf{F}$  is best represented as

$$\mathbf{F} = \mathbf{I} + a\eta \mathbf{e}_1 \otimes \mathbf{e}_1 + b\eta \mathbf{e}_2 \otimes \mathbf{e}_2 + b\eta \mathbf{e}_3 \otimes \mathbf{e}_3 \quad (19)$$

where  $a$  and  $b$  are constants with  $a > b$ .

In Fig. 7, we plot  $F_{xx}$ ,  $F_{yy}$ , and  $F_{zz}$  and the bi-layer system compressive strain equivalent ratio  $\epsilon_{xx}/\epsilon_{yy}$  with respect to  $1/\sqrt{\kappa}$  at the end of multiple simulations. In this plot, we can clearly see the transition between transversely isotropic ( $1/\sqrt{\kappa}$  is small) and isotropic ( $1/\sqrt{\kappa}$  is large) growth. Since we are most interested in  $\kappa$  within the range  $\kappa \approx 2-4$ , we are clearly most interested in the corresponding intermediate ranges of  $\epsilon_{xx}/\epsilon_{yy}$ . The results in this

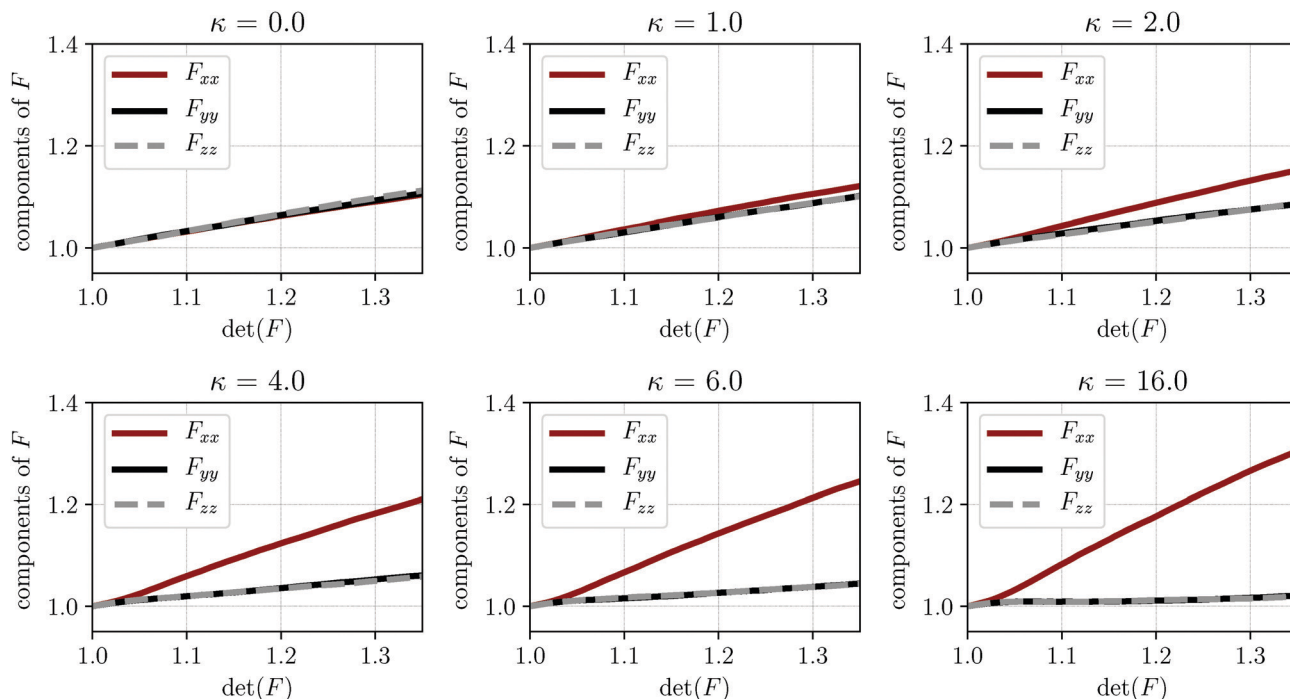


Fig. 6 Plots of the components of approximate deformation gradient  $F_{xx}$ ,  $F_{yy}$ , and  $F_{zz}$  with respect to approximate volume change  $\det \mathbf{F}$  for varying  $\kappa$ . Each simulation begins with a  $3 \times 3 \times 3$  block of cells and ends once the number of cells has doubled. Each curve represents the average of 300 simulations and off-diagonal terms are not plotted because they average to 0.

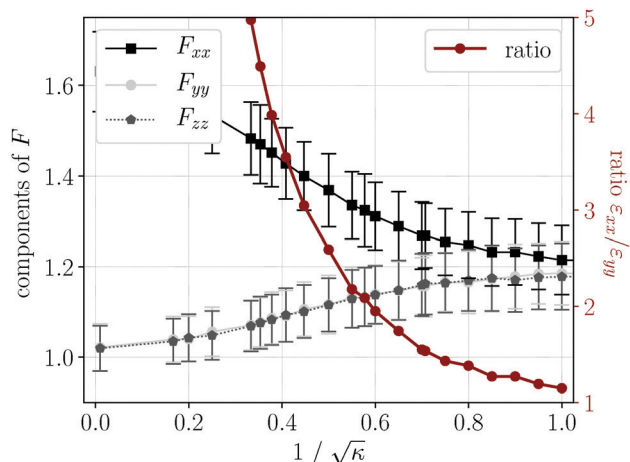


Fig. 7 Plots of final simulation results once the initial cell number has doubled. The left axis shows the components of approximate deformation gradient  $F_{xx}$ ,  $F_{yy}$ , and  $F_{zz}$  with respect to  $1/\sqrt{\kappa}$  while the right axis shows the ratio  $\lambda_x/\lambda_y$  (identical to  $\lambda_x/\lambda_z$ ) with respect to  $1/\sqrt{\kappa}$ . Because the plots in Fig. 6 are nearly linear, simulation results at one point in time are a meaningful representation. Each point shows the mean and standard deviation of 300 simulations.

section lead us to consider how the physically relevant form of  $\mathbf{F}$  represented in eqn (19) will manifest itself on the macroscale.

### 3.2 Oriented cell division with asynchronous cell growth leads to a uniaxial buckling mode

From Section 3.1, we generate a transversely isotropic tensor  $\mathbf{F}$  driven by oriented cell division. Now, we are prepared to

investigate the buckled shape of the system at the onset of the instability for physically relevant ratios of equivalent compressive strain  $\epsilon_{xx}/\epsilon_{yy}$ . In Section 2.3, we described our methodology for computing the buckled shape at the onset of the instability for a three-dimensional bilayer system with anisotropic growth. In Fig. 8, we show the results of the analysis. When compression is equi-biaxial, the buckled shape has a characteristic checkerboard pattern. Otherwise, the uniaxially buckled shape is the first to emerge. This is consistent with results reported in the literature.<sup>35–37</sup> In the context of cerebellar morphogenesis, this result is striking because it shows that even for “intermediate” ratios of  $\epsilon_{xx}/\epsilon_{yy}$ , equivalent to the growth described in eqn (19), the buckled shape at the onset of the instability is uniaxial. Specifically, a uniaxial mode with wrinkles perpendicular to the dominant direction of colony expansion will arise. Furthermore, the tissue-scale analysis shows that if all the cells grew perfectly in sync, the uniaxial mode may not develop because the buckling instability could be triggered by the entire cell population doubling in size before a cell division event would have the opportunity to produce population scale anisotropy. Our multi-scale model directly ties the observed pattern of oriented cell division with predominant division plane perpendicular to the anterior-posterior direction<sup>6</sup> to the characteristic oriented parallel grooves of the cerebellum.

In Fig. 9, we show the results of using our computational framework to more specifically simulate the developing cerebellum. First, we randomly generate cell division plane orientations to match the experimental observations detailed in Legué *et al.*<sup>6</sup> Then, we run multiple agent-based simulations and

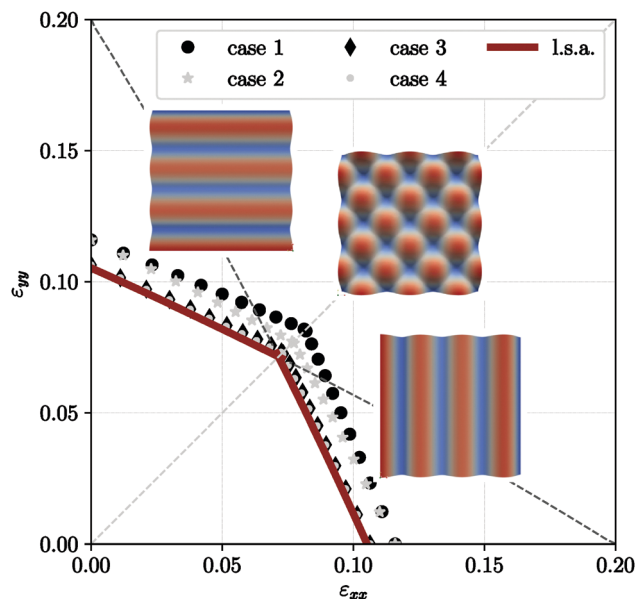


**Fig. 8** This plot shows the values of pairs of compressive strain ( $\epsilon_{xx}, \epsilon_{yy}$ ) at the onset of the instability from both the linear stability analysis (red line labeled l.s.a) and representative numerical results. For the numerical results, “case 1” refers to film growth only with growth in the  $\mathbf{e}_3$  direction, “case 2” refers to film growth only with no growth in the  $\mathbf{e}_3$  direction, “case 3” refers to film and substrate growth with growth in the  $\mathbf{e}_3$  direction, and “case 4” refers to film and substrate growth with no growth in the  $\mathbf{e}_3$  direction. The numerical results are obtained via eigenvalue analysis in isogeometric analysis simulations.<sup>33,34</sup> The dashed lines highlight the symmetry in both the analytical and numerical solutions. The qualitatively representative results pictured are for stiffness ratio  $E_f/E_s = 10$  and  $\epsilon_{yy} > \epsilon_{xx}$ ,  $\epsilon_{xx} = \epsilon_{yy}$ , and  $\epsilon_{xx} > \epsilon_{yy}$  clockwise. In our model of the cerebellum, the uniaxial mode will arise for all scenarios where  $\epsilon_{xx} > \epsilon_{yy}$ .

compute the growth induced deformation gradient  $\mathbf{F}$ . Finally, we implement the growth induced deformation  $\mathbf{F}$  in a tissue

scale isogeometric analysis model of a cylindrically curved domain. In Fig. 9d, we simulate a small amount of post-buckling deformation, essentially the initiation of cerebellar folds. These results strengthen the connection between experimentally observed oriented cell division and cerebellar morphogenesis.

## 4 Conclusion

The main objective of this work was to explore the connection between oriented cell division and cerebellar morphology. To do this, we began in Section 2.1 with an agent-based cell model where the algorithms for cell growth and division are selected to capture experimentally observed behavior. Then, in Section 2.2, we introduced a strategy for propagating the results of our agent-based model to a macroscale continuum model. Finally, in Section 2.3, we introduced our solution method for analyzing the buckled shape of the cerebellar cortex given the anisotropic film growth driven by oriented cell division. From this analysis, we found that physically realistic oriented cell division leads to a macroscale uniaxial first instability mode that is consistent with the morphology of the cerebellum. Notably, this is true even though physically realistic oriented cell division does not lead to entirely uni-directional anisotropic growth.

The ideas presented here are a starting point for future computational investigation. In particular, here we only consider instability initiation in our tissue-scale investigation. Further exploration of substantial post-buckling behavior is a challenging and compelling problem. Notably, once the initial instability is established, anchoring centers form at the base of each fissure and significant coordinated change on the cellular scale occurs.<sup>5</sup> Therefore, additional non-linear mechanisms must be included in the computational model to properly capture the full formation and post-buckling evolution of cerebellar folds.

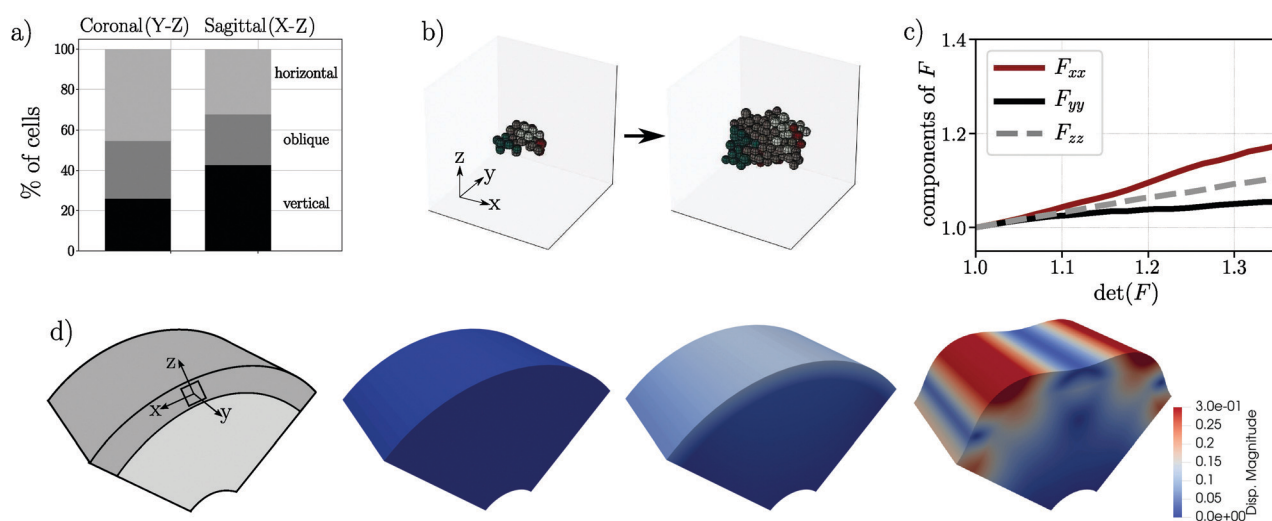


**Fig. 9** (a) The cell division angle is drawn from a probability distribution chosen to appear similar to the experimental results in Legu e *et al.*;<sup>6</sup> (b) illustrated results of a single simulation with the division angle drawn from the distribution shown in (a); (c) a plot of the components of  $\mathbf{F}$  generated with the same method as the results shown in Fig. 6; (d) the results of a tissue scale isogeometric analysis simulation where the growth induced deformation gradient shown in (c) is applied to the outer layer of a cylindrically curved domain.

Though elastic instability likely explains the initiation of folds, elastic deformation alone likely cannot explain the full process of cerebellar morphogenesis. Future work will build on this initial computational framework to move significantly beyond instability initiation.

In future work, the agent-based model could be adapted to capture a more physiological cell behavior through calibration with further experimental data and through the incorporation of additional physical phenomena such as cell migration and the occurrence of multiple cell shapes and types with extracellular fibers. On the continuum scale, further multi-physics<sup>38–40</sup> computational analysis with a tri-layer exact geometry with material anisotropy would also enhance our conclusions and our understanding of the mechanics driving cerebellar morphogenesis. Beyond the physiological case, this multi-scale modeling framework could be used to understand how genetically driven changes that are known to influence cell growth and cell division subsequently alter cerebellar morphogenesis in the pathological case. Ultimately, advanced future work can take advantage of the freedom provided by the computational setting to implement coupled simulations across multiple scales and explore the post-buckling behavior of the developing cerebellum on the macroscopic scale as an emergent property of cellular division on the microscopic scale.

## Conflicts of interest

There are no conflicts to declare.

## Appendix

The purpose of the appendix is to provide further detail to the models introduced in Section 2. Further information relevant to Section 2.1 is provided in Section A.1, and further information relevant to Section 2.3 is provided in Section A.2.

### A.1 Agent-based cell model

Here we elaborate on the agent-based model introduced in Section 2.1. We briefly provide the set of equations necessary to implement our model. The mechanical components of the agent-based model are based on peridynamics, a theoretical and computational framework that is implemented numerically as a mesh-free method where each node represents an individual cell.<sup>41,42</sup> Further information is also available in our prior work and in the broader peridynamics literature.<sup>24,43–46</sup>

To begin, we introduce the concept of baseline cell interaction distance  $\delta^*$  defined as

$$\delta_j^* = 2(1 + g_j)\delta_0 r_0. \quad (20)$$

where  $g$  is radial growth,  $r_0$  is initial radius, and  $\delta_0$  is a constant chosen such that cells only interact with their immediate neighbors. Then, we define the horizon of node  $j$ ,  $\mathcal{H}_j$ , as

$$\mathcal{H}_j = \{k \mid \|\mathbf{y}_j - \mathbf{y}_k\| < \delta_j^*\}. \quad (21)$$

where  $\mathbf{y}_j$  is the position of node  $j$  in the current configuration. We also introduce the concept of dual horizon  $\mathcal{H}'$  as

$$\mathcal{H}'_j = \{k \mid j \in \mathcal{H}_k\}. \quad (22)$$

The discrete form of the equation of motion at static equilibrium is then written as

$$0 = \sum_{k \in \mathcal{H}'_j} \mathbf{f}_{jk}(\mathbf{y}_j, \mathbf{y}_k) \Delta V_k - \sum_{k \in \mathcal{H}_j} \mathbf{f}_{kj}(\mathbf{y}_j, \mathbf{y}_k) \Delta V_k \quad (23)$$

where  $\Delta V$  is the growth adjusted nodal volume defined as

$$\Delta V_j = (1 + g_j)^n \Delta V_j^0 \quad (24)$$

and  $\mathbf{f}$  is the force density. The remainder of the equations in this appendix are introduced in order to define force density, analogous to defining a constitutive law. We define the stretch free separation distance between nodes as

$$\|\xi_{jk}\| = (1 + g_j)r_j + (1 + g_k)r_k \quad (25)$$

where  $r$  is cell radius and  $g$  is radial growth. Then, we define the stretch between nodes  $j$  and  $k$  as

$$s_{jk} = \frac{\|\mathbf{y}_k - \mathbf{y}_j\| - \|\xi_{jk}\|}{\|\xi_{jk}\|} \quad (26)$$

which is used to define bond damage  $\gamma_{jk}$  as

$$\gamma_{jk} = \begin{cases} 1 & \text{if } s < s_{\max} \\ 0 & \text{otherwise} \end{cases} \quad (27)$$

where  $s_{\max}$  is the maximum allowable stretch. This enters the influence function  $\omega$  as

$$\omega_{jk} = \gamma_{jk}. \quad (28)$$

We then define horizon weighted volume  $m$  as

$$m_j = \sum_{k \in \mathcal{H}_j} \omega_{jk} \|\xi_{jk}\|^2 \Delta V_k. \quad (29)$$

We define bond elongation  $e$  as

$$e_{jk} = \|\mathbf{y}_k - \mathbf{y}_j\| - \|\xi_{jk}\| \quad (30)$$

dilation  $\theta$  as

$$\theta_j = \frac{n}{m_j} \sum_{k \in \mathcal{H}_j} \omega_{jk} \|\xi_{jk}\| e_{jk} \Delta V_k \quad (31)$$

and deviatoric bond elongation  $e^d$  as

$$e_{jk}^d = e_{jk} - \frac{\theta_j \|\xi_{jk}\|}{n} \quad (32)$$

where  $n = 3$  is the dimension. Then, we define the magnitude of force density that arises at node  $k$  due to node  $j$  as

$$t_{kj} = \frac{n\kappa\theta_j}{m_j} \omega_{jk} \|\xi_{jk}\| + \frac{n(n+2)\mu}{m_j} \omega_{jk} e_{jk}^d \quad (33)$$

Table 1 Parameters used to implement the cellular scale simulations

Parameter	Value	Source
$E$	1 kPa	Plausible value
$\nu$	0.45	Nearly incompressible material
$r_0$	10 $\mu\text{m}$	Approximate cell size
$\delta_0$	1.05	Horizon size parameter
$s_{\text{max}}$	1.15	Fixed value consistent with previous work <sup>24</sup>

where  $\kappa$  and  $\mu$  are the Lamé parameters. Finally, force density is computed as

$$\mathbf{f}_{jk}(\mathbf{y}_j, \mathbf{y}_k) = t_{jk} \cdot \frac{\mathbf{y}_k - \mathbf{y}_j}{\|\mathbf{y}_k - \mathbf{y}_j\|}$$

$$\mathbf{f}_{kj}(\mathbf{y}_j, \mathbf{y}_k) = t_{kj} \cdot \frac{-(\mathbf{y}_k - \mathbf{y}_j)}{\|\mathbf{y}_k - \mathbf{y}_j\|}. \quad (34)$$

In Table 1 we list the parameters chosen for the simulations presented in Section 3.1 of this paper. After every step of algorithmically applied cell behavior (*i.e.* cell growth or cell division), the entire system is relaxed back to mechanical equilibrium defined by eqn (23) using an adaptive dynamic relaxation procedure.<sup>47</sup>

## A.2 Incremental stability analysis of a three-dimensional neo-Hookean bilayer under anisotropic compression

The equations governing the instability problem for the bilayer are derived from the exact solutions to the incremental equations of equilibrium in the neighborhood of a finite solution. As introduced in eqn (11), the contributions to free energy function of a neo-Hookean material are simply defined as

$$W(\mathbf{F}) = \frac{\mu}{2}(\mathbf{F} : \mathbf{F} - 3) \quad \text{and} \quad G = J - 1. \quad (35)$$

Here we consider the uniform stretches  $\lambda$ ,  $\eta$ , and  $\gamma$  in the  $X_1$ ,  $X_2$ , and  $X_3$  directions, respectively. The deformation gradient  $\mathbf{F}$  is defined as

$$\mathbf{F} = \lambda \mathbf{e}_1 \otimes \mathbf{e}_1 + \eta \mathbf{e}_2 \otimes \mathbf{e}_2 + \gamma \mathbf{e}_3 \otimes \mathbf{e}_3 \quad (36)$$

and the first Piola–Kirchhoff stress  $\mathbf{P}$  is computed as  $\mathbf{P} = \mu \mathbf{F} - p \mathbf{F}^{-T}$  in the homogeneously deformed state prior to the onset of the instability. The incremental first Piola–Kirchhoff stress  $\delta \mathbf{P}$  is defined in eqn (13) as  $\delta \mathbf{P} = \frac{\partial^2 W}{\partial \mathbf{F}^2} : \delta \mathbf{F} - \delta p \mathbf{F}^{-T} + p \mathbf{F}^{-T} \delta \mathbf{F}^T \mathbf{F}^{-T}$ .

The equilibrium equation  $\text{Div} \delta \mathbf{P} = 0$  is written in terms of  $\mathbf{F}$  defined in eqn (36) as

$$\frac{p + \lambda^2 \mu}{\lambda^2} u_{1,11} - \frac{\delta p_{,1}}{\lambda} + \mu u_{1,22} + p \frac{u_{2,12}}{\lambda \eta} + \mu u_{1,33} + p \frac{u_{3,13}}{\lambda \gamma} = 0$$

$$\mu u_{2,11} + p \frac{u_{1,21}}{\lambda \eta} + \frac{p + \eta^2 \mu}{\eta^2} u_{2,22} - \frac{\delta p_{,2}}{\eta} + \mu u_{2,33} + p \frac{u_{3,23}}{\eta \gamma} = 0 \quad (37)$$

$$\mu u_{3,11} + p \frac{u_{1,31}}{\lambda \gamma} + \mu u_{3,22} + p \frac{u_{2,32}}{\eta \gamma} + \frac{p + \gamma^2 \mu}{\gamma^2} u_{3,33} - \frac{\delta p_{,3}}{\gamma} = 0$$

and the incompressibility constraint is written as

$$\frac{u_{1,1}}{\lambda} + \frac{u_{2,2}}{\eta} + \frac{u_{3,3}}{\gamma} = 0. \quad (38)$$

The Lagrange multiplier  $p$  is determined by the traction-free surface condition  $P_{33} = 0$ , specifically  $P_{33} = \mu \gamma - p \gamma^{-1} = 0$ , which leads to  $p = \mu \gamma^2$ . The form of the infinitesimal perturbations in the film  $\mathbf{u}$  and  $\delta p$  are then given as

$$u_1^f = (A_1^f e^{r_1 X_3} + A_2^f e^{r_2 X_3} + A_3^f e^{r_3 X_3} + A_4^f e^{r_4 X_3}) \sin(k X_1) \cos(\rho X_2)$$

$$u_2^f = (B_1^f e^{r_1 X_3} + B_2^f e^{r_2 X_3} + B_3^f e^{r_3 X_3} + B_4^f e^{r_4 X_3}) \cos(k X_1) \sin(\rho X_2)$$

$$u_3^f = (C_1^f e^{r_1 X_3} + C_2^f e^{r_2 X_3} + C_3^f e^{r_3 X_3} + C_4^f e^{r_4 X_3}) \cos(k X_1) \cos(\rho X_2)$$

$$\delta p^f = \mu_f (D_1^f e^{r_1 X_3} + D_2^f e^{r_2 X_3} + D_3^f e^{r_3 X_3} + D_4^f e^{r_4 X_3}) \cos(k X_1) \cos(\rho X_2). \quad (39)$$

Then, we insert the perturbations given in eqn (39) into the equilibrium equation eqn (37) and the incompressibility constraint in eqn (38), and solve for the non trivial solutions of  $r$ . The non trivial solutions of  $r$  are

$$r_1 = \sqrt{\gamma^2 \left( \frac{k^2}{\lambda^2} + \frac{\rho^2}{\eta^2} \right)} \quad r_2 = \sqrt{k^2 + \rho^2} \quad (40)$$

$$r_3 = -r_2 \quad r_4 = -r_1.$$

Substituting eqn (39) including all solutions of  $r$  into the incremental equilibrium equation, eqn (37), we are left with the unknown coefficients  $A_2^f$ ,  $A_3^f$ ,  $B_2^f$ ,  $B_3^f$ ,  $D_1^f$ , and  $D_4^f$ . For the film ( $0 \leq X_3 \leq h$ ) with the shear modulus  $\mu_f$ , we enforce  $\delta \mathbf{P} = 0$  at the surface  $X_3 = h$  due to the traction free boundary condition as

$$\tilde{\mathbf{M}} \begin{bmatrix} A_2^f \\ B_2^f \\ D_1^f \end{bmatrix} = \tilde{\mathbf{N}} \begin{bmatrix} A_3^f \\ B_3^f \\ D_4^f \end{bmatrix} \quad (41)$$

where

$$\mathbf{M} = \begin{pmatrix} r_2 + \frac{\gamma^2 k^2}{r_2 \lambda^2} & \frac{\gamma^2 \rho k}{r_2 \lambda \eta} & \frac{2r_1 k}{\alpha_1 \lambda} \\ \frac{k \rho \gamma^2}{r_2 \lambda \eta} & r_2 + \frac{\rho^2 \gamma^2}{r_2 \eta^2} & \frac{2\rho r_1}{\alpha_1 \eta} \\ -\frac{2k\gamma}{\lambda} & -\frac{2\rho\gamma}{\eta} & \frac{2r_1^2}{\alpha_1 \gamma} - \frac{1}{\gamma} \end{pmatrix} \quad (42)$$

$$\mathbf{N} = \begin{pmatrix} r_3 + \frac{\gamma^2 k^2}{r_3 \lambda^2} & \frac{\gamma^2 \rho k}{r_3 \lambda \eta} & \frac{2r_4 k}{\alpha_4 \lambda} \\ \frac{k \rho \gamma^2}{r_3 \lambda \eta} & r_3 + \frac{\rho^2 \gamma^2}{r_3 \eta^2} & \frac{2\rho r_4}{\alpha_4 \eta} \\ -\frac{2k\gamma}{\lambda} & -\frac{2\rho\gamma}{\eta} & \frac{2r_4^2}{\alpha_4 \gamma} - \frac{1}{\gamma} \end{pmatrix}$$

$$\tilde{\mathbf{M}} = \mathbf{M} \mathbf{E}_1 \quad \text{with } \mathbf{E}_1 = \text{diag}(e^{r_2 h}, e^{r_2 h}, e^{r_1 h})$$

$$\tilde{\mathbf{N}} = \mathbf{N} \mathbf{E}_2 \quad \text{with } \mathbf{E}_2 = \text{diag}(e^{r_3 h}, e^{r_3 h}, e^{r_4 h})$$

$\alpha_1 = r_1^2 - \rho^2 - k^2$  and  $\alpha_4 = r_4^2 - \rho^2 - k^2$ . Next, we compute  $u_1^f, u_2^f$ , and  $u_3^f$  at the film–substrate interface  $X_3 = 0^+$ . Using eqn (41), we write it in terms of  $[A_2^f, B_2^f, D_1^f]^T$  as

$$\begin{bmatrix} u_1^f \\ u_2^f \\ u_3^f \end{bmatrix} = \mathbf{T}(\mathbf{K} + \mathbf{L}\mathbf{S}) \begin{bmatrix} A_2^f \\ B_2^f \\ D_1^f \end{bmatrix} \quad (43)$$

where

$$\mathbf{K} = \begin{pmatrix} 1 & 0 & \frac{-k}{\alpha_1 \lambda} \\ 0 & 1 & \frac{-\rho}{\alpha_1 \eta} \\ \frac{-\gamma k}{r_2 \lambda} & \frac{-\gamma \rho}{r_2 \eta} & \frac{r_1}{\alpha_1 \gamma} \end{pmatrix}$$

$$\mathbf{L} = \begin{pmatrix} 1 & 0 & \frac{-k}{\alpha_4 \lambda} \\ 0 & 1 & \frac{-\rho}{\alpha_4 \eta} \\ \frac{-\gamma k}{r_3 \lambda} & \frac{-\gamma \rho}{r_3 \eta} & \frac{r_4}{\alpha_4 \gamma} \end{pmatrix}$$

$$\mathbf{T} = \begin{pmatrix} \sin(kX_1) \cos(\rho X_2) & 0 & 0 \\ 0 & \cos(kX_1) \sin(\rho X_2) & 0 \\ 0 & 0 & \cos(kX_1) \cos(\rho X_2) \end{pmatrix}$$

$$\mathbf{S} = \tilde{\mathbf{N}}^{-1} \tilde{\mathbf{M}}. \quad (44)$$

Using eqn (41) and (43), we relate the incremental first Piola–Kirchhoff stress at the film–substrate interface  $X_3 = 0$  to the perturbations as

$$\begin{bmatrix} \delta P_{13}^f \\ \delta P_{23}^f \\ \delta P_{33}^f \end{bmatrix} = \mu_f \mathbf{T} \mathbf{G} \mathbf{T}^{-1} \begin{bmatrix} u_1^f \\ u_2^f \\ u_3^f \end{bmatrix} \quad (45)$$

where  $\mathbf{G} = (\mathbf{M} + \mathbf{N}\mathbf{S})(\mathbf{K} + \mathbf{L}\mathbf{S})^{-1}$ . Turning now to the substrate with shear modulus  $\mu_s$ , we take advantage of the assumption that the substrate is an infinite half-space. The general solution in eqn (39) will apply to the substrate with  $r_3 = 0$  and  $r_4 = 0$  since the perturbations are required to vanish as  $X_3 \rightarrow -\infty$ . Similar to eqn (45), the incremental first Piola–Kirchhoff stress at the film–substrate interface  $X_3 = 0^-$  is written as

$$\begin{bmatrix} \delta P_{13}^s \\ \delta P_{23}^s \\ \delta P_{33}^s \end{bmatrix} = \mu_s \mathbf{T} \mathbf{M} \mathbf{K}^{-1} \mathbf{T}^{-1} \begin{bmatrix} u_1^s \\ u_2^s \\ u_3^s \end{bmatrix}. \quad (46)$$

Finally, we enforce the condition that the traction and the perturbations must be consistent across the film–substrate interface  $X_3 = 0^+$  and  $X_3 = 0^-$ , i.e. the relationship

$$\begin{bmatrix} u_1^s \\ u_2^s \\ u_3^s \end{bmatrix} = \begin{bmatrix} u_1^f \\ u_2^f \\ u_3^f \end{bmatrix} \quad (47)$$

must hold which allows us to subsequently equate eqn (45) and (46) as

$$\left( \mathbf{M} \mathbf{K}^{-1} - \frac{\mu_f}{\mu_s} \mathbf{G} \right) \begin{bmatrix} u_1^f \\ u_2^f \\ u_3^f \end{bmatrix} = \mathbf{Q} \begin{bmatrix} u_1^f \\ u_2^f \\ u_3^f \end{bmatrix} = 0. \quad (48)$$

The eigenvalue problem to detect the onset of the instability and the associated buckled mode is then defined as  $\det(\mathbf{Q}) = 0$ . The first eigenmode is calculated by minimizing the critical strain  $\epsilon_{xx} = 1 - \lambda$  over all possible values of  $k$  and  $\rho$  that satisfy  $\det(\mathbf{Q}) = 0$ , given the applied directional stretch  $\eta$  defined in eqn (36). In Fig. 8, we observe that the critical strain is associated with uniaxial sinusoidal wrinkling in the dominant direction of applied compression, i.e.  $k/\rho \rightarrow \infty$ . It is only when  $\lambda = \eta$  that the equi-biaxial instability mode arises.

## Acknowledgements

Financial support for this research was provided by the National Science Foundation Graduate Research Fellowship under Grant No. DGE-114747 and the National Science Foundation CAREER Award CMMI-1553638. This support is gratefully acknowledged.

## References

- 1 K. Leto, M. Arancillo, E. B. E. Becker, A. Buffo, C. Chiang, B. Ding, W. B. Dobyns, I. Dusart, P. Haldipur, M. E. Hatten, M. Hoshino, A. L. Joyner, M. Kano, D. L. Kilpatrick, N. Koibuchi, S. Marino, S. Martinez, K. J. Millen, T. O. Millner, T. Miyata, E. Parmigiani, K. Schilling, G. Sekerková, R. V. Sillitoe, C. Sotelo, N. Uesaka, A. Wefers, R. J. T. Wingate and R. Hawkes, *Cerebellum*, 2015, **15**, 789–828.
- 2 R. V. Sillitoe and A. L. Joyner, *Annu. Rev. Cell Dev. Biol.*, 2007, **23**, 549–577.
- 3 J. D. Corrales, G. L. Rocco, S. Blaess, Q. Guo and A. L. Joyner, *Development*, 2004, **131**, 5581–5590.
- 4 J. D. Corrales, S. Blaess, E. M. Mahoney and A. L. Joyner, *Development*, 2006, **133**, 1811–1821.
- 5 A. Sudarov and A. L. Joyner, *Neural Dev.*, 2007, **2**, 26.
- 6 E. Legué, E. Riedel and A. L. Joyner, *Development*, 2015, **142**, 1661–1671.
- 7 E. Lejeune, A. Javili, J. Weickenmeier, E. Kuhl and C. Linder, *Soft Matter*, 2016, **12**, 5613–5620.
- 8 A. K. Lawton, T. Engstrom, D. Rohrbach, M. Omura, D. H. Turnbull, J. Mamou, T. Zhang, J. M. Schwarz and A. L. Joyner, *bioRxiv*, 2019, DOI: 10.1101/382887.

- 9 P. Ciarletta, V. Balbi and E. Kuhl, *Phys. Rev. Lett.*, 2014, **113**, 248101.
- 10 A. E. Shyer, T. Tallinen, N. L. Nerurkar, Z. Wei, E. S. Gil, D. L. Kaplan, C. J. Tabin and L. Mahadevan, *Science*, 2013, **342**, 212–218.
- 11 M. Ben Amar and A. Goriely, *J. Mech. Phys. Solids*, 2006, **53**, 2284–2319.
- 12 P. Ciarletta and M. Ben Amar, *Int. J. Non Linear Mech.*, 2012, **47**, 248–257.
- 13 S. Budday, P. Steinmann and E. Kuhl, *Front. Cell. Neurosci.*, 2015, **9**, 1–17.
- 14 E. Kuhl, *Nat. Phys.*, 2016, **12**, 533.
- 15 D. P. Richman, R. M. Stewart, J. W. Hutchinson and V. S. Caviness, *Science*, 1975, **189**, 18–21.
- 16 T. Tallinen, J. Y. Chung, F. Rousseau, N. Girard, J. Lefèvre and L. Mahadevan, *Nat. Phys.*, 2016, **12**, 588.
- 17 S. Verner and K. Garikipati, *Extreme Mech. Lett.*, 2018, **18**, 58–69.
- 18 T. A. Engstrom, T. Zhang, A. K. Lawton, A. L. Joyner and J. M. Schwarz, *Phys. Rev. X*, 2018, **8**, 041053.
- 19 A. L. Joyner, R. Willett and A. Lawton, *Development of the Cerebellum from Molecular Aspects to Diseases*, Springer, 2017.
- 20 M. A. Biot, *Mechanics of Incremental Deformations*, John Wiley and Sons, New York, 1965.
- 21 T. J. R. Hughes, J. A. Cottrell and Y. Bazilevs, *Comput. Methods Appl. Mech. Eng.*, 2005, **194**, 4135–4195.
- 22 G. An, Q. Mi, J. Dutta-Moscato and Y. Vodovotz, *Wiley Interdiscip. Rev.: Syst. Biol. Med.*, 2009, **1**, 159–171.
- 23 S. A. Silling, M. Epton, O. Weckner, J. Xu and E. Askari, *J. Elasticity*, 2007, **88**, 151–184.
- 24 E. Lejeune and C. Linder, *Biomech. Model. Mechanobiol.*, 2017, 1–17.
- 25 A.-C. Petit, E. Legué and J.-F. Nicolas, *Reprod., Nutr., Dev.*, 2005, **45**, 321–339.
- 26 J.-U. Kreft, G. Booth and J. W. Wimpenny, *Microbiology*, 1998, **144**, 3275–3287.
- 27 K. V. Mardia and P. E. Jupp, *Directional statistics*, John Wiley & Sons, 2009, vol. 494.
- 28 G. Ulrich, *Applied Statistics*, 1984, 158–163.
- 29 A. T. Wood, *Communications in statistics-simulation and computation*, 1994, **23**, 157–164.
- 30 E. Lejeune and C. Linder, *J. Theor. Biol.*, 2017, **418**, 1–7.
- 31 D. A. Van Valen, T. Kudo, K. M. Lane, D. N. Macklin, N. T. Quach, M. M. DeFelice, I. Maayan, Y. Tanouchi, E. A. Ashley and M. W. Covert, *PLoS Comput. Biol.*, 2016, **12**, e1005177.
- 32 M. Holland, B. Li, X. Feng and E. Kuhl, *J. Mech. Phys. Solids*, 2017, **98**, 350–365.
- 33 B. Dortdivanlioglu, A. Javili and C. Linder, *Comput. Methods Appl. Mech. Eng.*, 2017, **316**, 261–279.
- 34 A. Javili, B. Dortdivanlioglu, E. Kuhl and C. Linder, *Comput. Mech.*, 2015, **56**, 405–420.
- 35 X. Huang, B. Li, W. Hong, Y.-P. Cao and X.-Q. Feng, *J. Mech. Phys. Solids*, 2016, **94**, 88–104.
- 36 B. Audoly and A. Boudaoud, *J. Mech. Phys. Solids*, 2008, **56**, 2401–2421.
- 37 D. Breid and A. J. Crosby, *Soft Matter*, 2011, **7**, 4490–4496.
- 38 K. Garikipati, *J. Mech. Phys. Solids*, 2017, **99**, 192–210.
- 39 B. Dortdivanlioglu, A. Krischok, L. Beirão da Veiga and C. Linder, *Int. J. Numer. Methods Eng.*, 2018, **114**, 28–46.
- 40 B. Dortdivanlioglu and C. Linder, *J. Mech. Phys. Solids*, 2019, **125**, 38–52.
- 41 S. A. Silling, *J. Mech. Phys. Solids*, 2000, **48**, 175–209.
- 42 S. A. Silling and E. Askari, *Comput. Struct.*, 2005, **83**, 1526–1535.
- 43 E. Madenci and E. Oterkus, *Peridynamic theory and its applications*, Springer, 2014.
- 44 S. A. Silling and R. B. Lehoucq, *Adv. Appl. Mech.*, 2010, **44**, 73–168.
- 45 D. Littlewood, SAND Report, Sandia National Laboratories, Albuquerque, NM and Livermore, CA., 2015.
- 46 S. Oterkus, PhD thesis, The University of Arizona, 2015.
- 47 B. Kilic and E. Madenci, *Theor. Appl. Fract. Mech.*, 2010, **53**, 194–204.